ESA Climate Change Initiative – Fire_cci
D5.1 Climate Assessment Report (CAR)

Project Name	ECV Fire Disturbance: Fire_cci
Contract Nº	4000126706/19/I-NB
Issue Date	22/06/2022
Version	3.1
Author	Florent MOUILLOT, Wentao CHEN, Philippe CIAIS
Document Ref.	Fire_cci_D5.1_CAR_3.1
Document type	Public

To be cited as: Mouillot, F., Chen, W., Ciais, P. (2022) ESA CCI ECV Fire Disturbance: D5.1 Product Validation and Intercomparison Report, version 3.1. Available at: https://climate.esa.int/en/projects/fire/key-documents/

Project Partners

Prime Contractor/ Scientific Lead & Project Management	UAH – University of Alcala (Spain)
Earth Observation Team	UAH – University of Alcala (Spain) UPM – Universidad Politécnica de Madrid (Spain) CNR-IREA - National Research Council of Italy – Institute for Electromagnetic Sensing of the Environment (Italy)
System Engineering	BC – Brockmann Consult (Germany)
Climate Modelling Group	CNRS - National Centre for Scientific (France) VU – Vrije Universiteit Amsterdam (Netherlands)

Distribution

Affiliation	Name	Address	Copies
ESA	Clément Albergel (ESA)	clement.albergel@esa.int	electronic copy
Project Team	Emilio Chuvieco (UAH) M. Lucrecia Pettinari (UAH) Amin Khaïroun (UAH) Magí Franquesa (UAH) Consuelo Gonzalo (UPM) Ángel Mario García Pedrero (UPM) Dionisio Rodríguez Esparragón (UPM) Daniela Stroppiana (CNR) Matteo Sali (CNR) Thomas Storm (BC) Florent Mouillot (CNRS) Wentao Chen (CNRS) Philippe Ciais (CNRS) Guido van der Werf (VU)	emilio.chuvieco@uah.es mlucrecia.pettinari@uah.es amin.khairoun@uah.es magin.franquesa@uah.es consuelo.gonzalo@upm.es angelmario.garcia@upm.es dionisio.rodriguez@ulpgc.es stroppiana.d@irea.cnr.it sali.m@irea.cnr.it thomas.storm@brockmann-consult.de florent.mouillot@ird.fr wentao.chen@cefe.cnrs.fr philippe.ciais@lsce.ipsl.fr g.r.vander.werf@vu.nl	electronic copy

Summary

This document is the version 3.1 of the Climate Assessment Report for the Fire_cci project. It refers to Task 5, Work Package 5200 – Dynamic Vegetation Models. This document is a completely new version compared to the previous one, focusing on the user case of the applications of the ECV products. In this document, FireCCI51 and FireCCISFD20 are assessed through the development of fire patches from those products, and a comparison with previous datasets and applications in global fire regime analysis.

	Affiliation/Function	Name	Date
Prepared	CNRS	Florent Mouillot Wentao Chen Philippe Ciais	16/06/2022
Reviewed	UAH – Project Manager UAH - Science Leader	M. Lucrecia Pettinari Emilio Chuvieco	22/06/2022
Authorized	UAH - Science Leader	Emilio Chuvieco	22/06/2022
Accepted	ESA - Technical Officer	Clément Albergel	

This document is not signed. It is provided as an electronic copy.

Document Status Sheet

Issue	Date	Details
1.0	31/03/2017	First Document Issue
1.1	30/09/2017	Revised document, including answers to the comments on CCI-FIRE-EOPS-MM-17-0045, new analysis, and the inclusion and analysis of Sentinel-2 SFD BA information.
1.2	23/04/2018	Revised document, including answers to the comments on CCI-FIRE-EOPS-MM-18-0004, and new analysis of the MODIS Fire_cci v5.0 product.
1.3	22/06/2018	Revised document, including answers to the comments on CCI-FIRE-EOPS-MM-18-0159
1.4	16/11/2018	Update of the document
2.0	06/11/2020	Update of the whole content of the document
2.1	16/11/2020	Revised document, including answers to the comments on Fire_cci+_5.1_CAR_v2.0_RID
3.0	16/05/2022	Update of the whole content of the document
3.1	22/06/2022	Revised document addressing comments of ESA's TO.

Document Change Record

Issue	Date	Request	Location	Details
1.1	30/09/2017	ESA, LSCE-IRD	Summary Figures 3 and 4 Section 3.1 Section 3.2, Section 4. Conclusion	Update of the summary of the document. Figures updated to include MCD64A1. Minor changes in the text The sections have been expanded with new analyses and new datasets. The conclusions were updated to include the new analyses performed.
1.2	23/04/2018	ESA, LSCE-IRD	Summary Section 1 Section 2 Section 3 Section 3.1	Update of the summary of the document. Small changes in the text to address MODIS Fire_cci v5.0. Parameter units corrected, and ellipse main features expanded. Text expanded Small changes in the text.

			Section 3.2 Section 4.1 Section 4.2.1 Section 4.2.2 Section 4.4 Section 6	The analysis was changed to include MCD64A1 C6 instead of MCD45A1 C5. The figures and text were updated. Small changes in the text. Text updated (was previously Section 4.2) New section added Added comparison of SFD and MCD64A1 Conclusions updated
1.3	22/06/2018	ESA, LSCE-IRD	All document Figure 1 Figure 5 Section 3.2	Inclusion of acronyms of the products. Figure updated Caption updated Clarification added to the first paragraph.
1.4	16/11/2018	LSCE-IRD	All document Sections 3.3, 5.3 Sections 4.2.1, 4.4 Section 4.2.2 Previous Sections 5.1 and 5.2 Section 6	Inclusion of FireCCI51 analysis New sections added Small changes in the text Text updated to include FireCCI51 Sections replaced by new Section 5.1 Text updated
2.0	06/11/2020	MPIM	All document	All document updated
2.1	16/11/2020	ESA	Sections 2.1, 4.5.1 Section 3 Section 4.3 Sections 4.4.2, 5	Small changes in the text and Figure legends updated Table 2 expanded Text expanded Small changes in the text
3.0	16/05/2022	CNRS	All document	All document updated
3.1	22/06/2022	ESA UAH	Sections 3.1.1, 4.2.2, 5, 6 Section 3.2.1 Section 3.2.2	Small changes in the text Figure 2 updated Text expanded, Figure 4 added

Table of Contents

List of Figures

List of Tables

1. Executive Summary

Global fire emissions for atmospheric chemistry models have relied on global burned area derived from remote sensing. Increasing higher spatial and temporal resolution in burned area datasets have recently allowed for fire patch identification by aggregating pixel-level information. This increasing level of information could provide substantial additional understanding of fire regimes, combustion processes and post-fire vegetation dynamic as a function of fire size or complexity. Among others, capturing fire patches could lead to a better understanding of extreme events as mega fires, their frequency by assessing fire size distribution, delivering their rate of spread and directional preferences, and their boundary complexity. Providing fire contours in countries where no fire information is available also became a keystone source of information for fire management planning.

Global burned area from coarse scale resolution remains however hardly reliable when considering small fires, leading to missed fires or gross fire shape. In addition, the time delay in burn date identification can bias pixel aggregation methods based on the spatial temporal threshold considered for two neighbouring pixels to belong to the same fire patch. The improved spatial resolution in FireCCI51 and FireCCISFD20 compared to previously available datasets might in turn increase the accuracy in fire patch number and shape.

We assessed here the FireCCI51 global fire dataset at 250m resolution and FireCCISFD20 at 20m resolution for the year 2019 in Africa capturing fire patches, following the previous global fire patch morphology database FRYv1.0 based on MCD641A1 and FireCCI41. We propose an updated pixel aggregation method allowing partitioning multiple and simultaneous fire starts merging into one final fire patch. Based on other available fire patch datasets, and user feedbacks and requirements received along the project, we also extended fire patch information compared to the previously delivered dataset FRYv1.0. We integrated fire ignition location as the minimum burn date of the fire patch and the rate of spread, two key information for climate modelling and fire hazard benchmarking derived from fire modules embedded in dynamic global vegetation models. The final shape file of each fire is also provided. This report describes the methods used, the dataset generated, a full comparison with previously delivered datasets as well some applications in global fire regime analysis.

2. Introduction

Global fire emissions massively rely on burned area derived from global remote sensing (van der Werf et al. 2017). Since the year 2000, monthly datasets at 0.5° resolution have provided burned area over the globe to be inserted in biogeochemical models simulating carbon emissions and greenhouse gases. By providing a global picture of the spatial, seasonal and interannual variability of the global burned area, these data also allowed for an increasing understanding of fire regimes and a benchmarking reference for process-based models simulating fires imbedded in global dynamic vegetation models (Hantson et al. 2016). The 500m pixel-resolution data was hardly used beside regional studies. However, the benefits of this information for identifying fire patches, and fire spread processes within these patches, recently emerged as a new perspective in pyrogeography and burned area modelling. The FRYv10 database initially delivered by Laurent et al. (2018) was derived from MCD64A1 and FireCCI41 to deliver fire patch location and morphological features from two sensors. The Global Fire Atlas was then delivered from MCD64A1 as a shape file dataset with fire spread information and dating (Andela et al.

2019). After analysing these datasets and their caveats, new pixel aggregation methods were proposed (Oom et al. 2016), mostly improving the detection of individual fire patches ignited independently at the same time but merging into one single large final burned area, but also single fires stepping ahead small fire by firebrands, by adding a spatial threshold so that non-neighbour pixels could belong to the same fire patch if they fall within that distance threshold. When analysing these datasets, a major issue remains the temporal threshold in the burn date difference to use and be considered for two neighbouring pixels as belonging to the same fire patch. Fire spread could be slow and take few days to spread from one pixel to its neighbour at 500m resolution, but burn date identification can be also highly biased to get a clean image to be used in the fire detection algorithm. Temporal thresholds of 3 to 14 days have been used. Moreno et al. (2020, 2021) tried and assessed the fire patch discrepancies between sensors and thresholds and identified major differences in the cloudy tropics and fair agreement with a 6-day threshold in North America. They also concluded that an increased temporal resolution would highly improve the fire patch identification and that a finer spatial resolution would allow for better shape characterisation.

We describe in this report the newly delivered global fire patch database based on FireCCI51, at 250m resolution, combining a better spatial and temporal resolution than MCD64A1 and FireCCI41. We also improved the fire patch characterization based on other fire patch databases and user feedbacks received from FRYv1.0. We also provide the fire patch database for Africa 2019 based on the FireCCISFD20 burned area product at 20m resolution from the Sentinel-2 sensor, as a new reference at fine resolution for comparison with coarser reference data.

3. FRYv2.0: a global fire patch morphology database from FireCCI51

3.1 Material and Methods

3.1.1 Pixel-level data

As input, we used three burned area datasets to produce fire patches. The first one is the FireCCI burned area pixel product version 5.1 (FireCCI51), based on the MODIS Collection 6 product at 250m resolution at the equator (MOD09GQ from the Terra satellite for daily surface reflectance, MOD09GA for data quality, and MCD14ML for thermal information), covering the period from 2001 to 2019 (Lizundia-Loiola et al., 2020). The burned area data is represented as the date of the first detection for each burned pixel, using a two-phase algorithm described in Lizundia-Loiola et al. (2020). In brief, the algorithm selects “seed” pixels of potential fires by using MODIS thermal anomalies and considering the relative drop in the near-infrared reflectance (the “seed” phase), then the candidate “seeds” go through a contextual region growing to obtain the entire burned patch (the “growing” phase). To account for the different vegetation covers within the same processing tile, adaptative burned-unburned thresholds are applied to each phase in cluster level. To provide land cover information for the final patch functional trait results, we used the land cover layer that comes with the burned area data. For each processed year, the land cover information is extracted from the CCI land cover map (CCI_LC v2.0.7) of the previous year. Since the CCI_LC v2.0.7 dataset over the period 2000-2015 had been used for the generation of original FireCCI51 dataset spanning from 2001 to 2018, the subsequent extension to 2019 also used the same land cover data for consistency. This means that the burned area maps of 2016 to 2019 use the CCI_LC v2.0.7 of 2015. At the moment of production of the original BA product, the land cover product v2.1.1 was not yet available (but it is now available through the Copernicus Climate Change Service), and for that reason it had not been used.

The second burned area dataset is the MCD64A1 Collection 6 BA product, derived from the Terra and Aqua satellite's on-board MODIS sensors (Giglio et al., 2016), which was also used in the previous FRY v1 datasets as input (Laurent et al., 2018). This product provides global burned area with a 463m resolution at the equator, with an extended time span from 2000 to 2019. As with the FireCCI51 product, the MCD64A1 Collection 6 BA product provides the burn date and its uncertainty for each burned pixel.

3.1.2 Pixel aggregation method

We used the date of the first detection (burned date or BD for short) of each pixel as the basic component to reconstruct fire patches (FPs). In a FP, all pixels are spatially connected with a queen neighbourhood, as well as temporally coherent, i.e. every pixel is adjacent to at least one another pixel so that the absolute difference of their BDs is equal to or below a fixed cut-off value (in days). Consequently, many such FPs may contain multiple clusters, each of which is formed by pixels of a common BD. Among these FPs, some may contain multiple ignition clusters, defined as clusters that have the earliest BDs among their neighbours. Such case is especially frequent among very large FPs. In reality, this may indicate several converging fire events, and therefore should be separated (Oom et al., 2016). Following Oom et al. (2016), we decided to separate large FPs in those cases into several smaller sub-FPs, each of which consists of several clusters of identical BD, such that each cluster had at most one neighbour cluster of a BD that was earlier than its own BD. In another word, in a sub-FP, each cluster of identical BD was either the ignition cluster, or a subsequent one "caused" by a single neighbour cluster of an earlier BD. As a result, each sub-FP formed a "causal" tree with clusters as node, and causal relationships went from the ignition cluster (root), through nodes with intermediate BDs, to the final clusters with the latest BDs. The resulted number of sub-FPs was therefore equal to the number of ignition points (Figure 1). We call these sub-FPs Single Ignition Fire Patches (SIFPs).

A maximal weakly connected components (MWCCs) approach was applied to construct the FPs. First, one-on-one neighbouring relationships among all pixels within a certain spatio-temporal window (explained below) were calculated based on the pixels' spatial coordinates. We then discarded any relationship involving two BDs with a difference larger than a cut-off value. The remaining neighbouring relationships were considered as contiguities between nodes (i.e., pixels). A simple breadth-first search was applied to these contiguities to find pixel groups as clusters of MWCCs. These pixel groups were then considered as FPs.

All of the three input datasets were provided as Geotiff maps that separate the global area into several tiles, in a monthly pace. Even so, each single tile still covered a large spatial expanse, so that it was not practical to fit the data of a single tile through the whole study period into a single run of computation. Therefore, we divided every Geotiff map by a 12×12 grid, and then regrouped all the resulted sub-tiles within a six-month fire season (i.e., from October of the previous year to March of the current year, or from April to September of the same year). These groups of sub-tiles were the spatio-temporal blocks on which the MWCC procedure was performed.

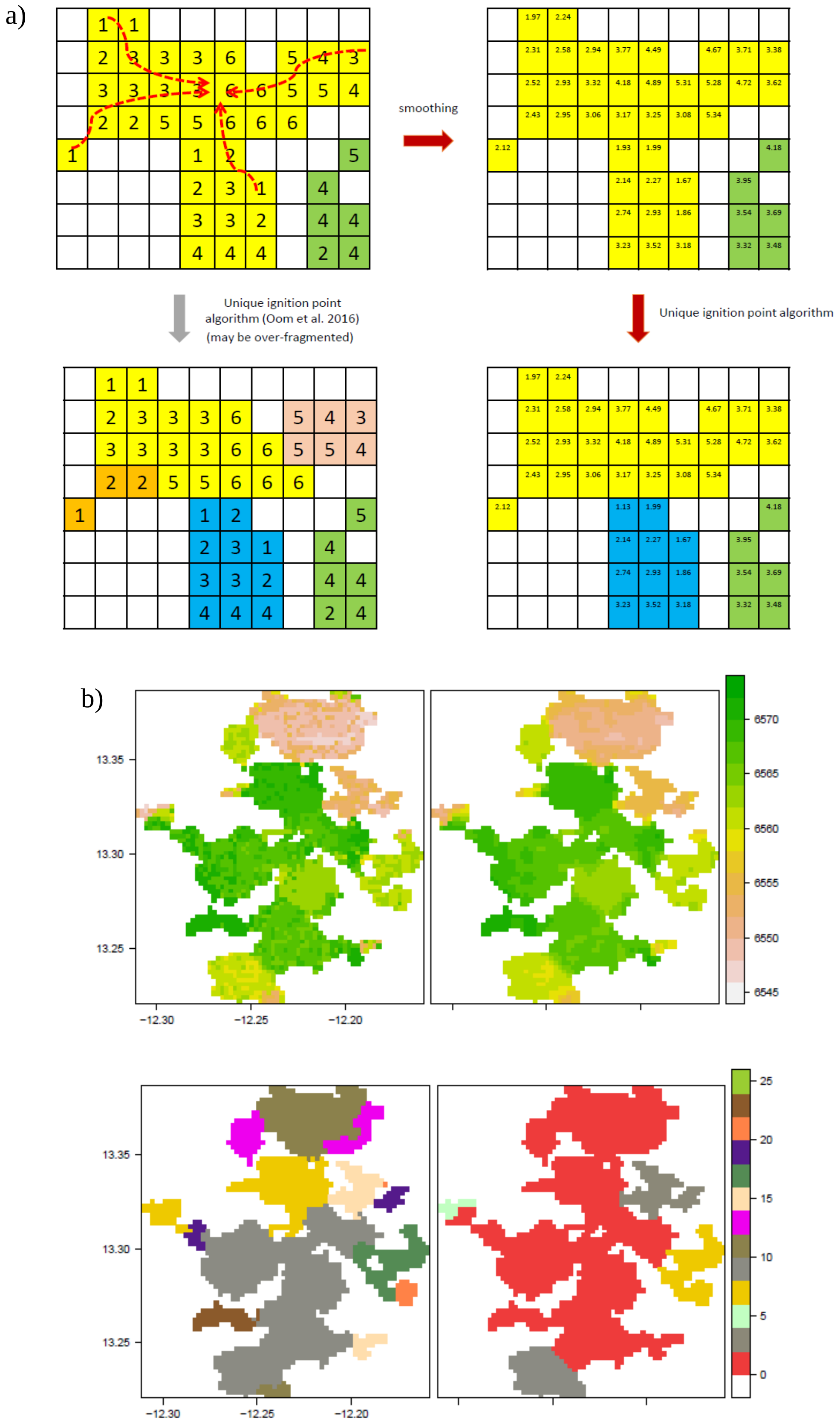

Figure 1: a) Schematic representation of the pixel aggregation methodology used in FRYv2. b) Example of fire patches generated from raw and smoothed burn dates.

As a result, FPs crossing sub-tiles, tiles or fire seasons were artificially fragmented. We designed an extra procedure to put these fragments back together. Before applying the MWCC procedure, we marked all pixels lying on the edges of sub-tiles, tiles and fire seasons (i.e., having a BD that lied within X days after or before the beginning or end date of a fire season, respectively, where X is the cut-off value). After the first round of MWCC computation, we extracted the FPs that contained any of the marked pixels and saved them separately according to the types of edge pixels they contained. The remaining FPs were saved as results. In the "piece-back" step, the FPs with sub-tile-edge pixels of the same sub-tile region were the first to go through another slightly modified MWCC procedure, in order to reconstruct FPs divided by sub-tiling. The MWCC procedure was slightly different from the previous one, because at this step, there was no need to consider all the pixels of the FPs, but only the edge pixels, in order to save memory space. By computing only on the edge pixels, the MWCC procedure established the contiguity between FP fragments. Subsequently, connected FP fragments were pieced together into new FPs. Again, any FPs containing fire-season- or tile- edge pixels among the new FPs were saved separately for the next steps, the remaining new FPs were saved as results. Similar procedures were performed on the FPs containing fire-season- or tile- edge pixels, respectively. The final results were then obtained with no FP fragments introduced by the block-making steps.

To decompose the FPs obtained as described above into SIFPs, we adopted the approach of Oom et al. (2016) with some slight modifications. Our approach was a trade-off between separating converging FPs as much as possible and avoiding over-fragmenting due to BD uncertainty. We began by smoothing the BDs of the original pixels with a 3 by 3 (cells) window, by applying a Gaussian filter to the BDs that were earlier than- or equal to the BD of the central pixel. Pixels in the 3 by 3 window with a BD later than the centre pixel's were not considered to avoid filling BD gaps that would be used to separate FPs in the next steps. This step aimed to avoid over-splitting FPs with many small single-BD clusters, and at the same time keeping the borders between distinct sub-clusters. For any ordered pair of pixels (A, B), we then established a contiguity as in the previous FP-construction procedure with the same cut-off value. In order to establish the causal relationships among pixels, we sorted the contiguities according to the pixels' smoothed BDs: "same" days; "causal" if days (the fire could only have been propagated from A to B); "backwards" if days (the fire could only have been propagated from B to A). We then discarded all "backwards" contiguities and kept only the "same" and the "causal" ones. Considering only the "same" contiguities, pixel clusters where neighbouring pixels had close BDs were established with a simple breadth-first search. "Causal" contiguities were then used to link the clusters obtained above to form SIFPs using breadth-first search at cluster level. If a cluster had multiple possible "causal" clusters at its neighbourhood, we randomly drew one among them, the probability of a candidate "causal" cluster being drawn was proportional to the number of pixels lying at the border between it and the cluster in question (Figure 1). Finally, all SIFPs that were smaller than 100 ha were regrouped with neighbouring larger SIFPs, in order to avoid over-fragmentation of FPs.

3.1.3 Patch morphology

Fire patches functional traits (FPFTs) in the FRY v2 dataset were calculated based on both the FPs and SIFPs obtained from the previous steps, using R packages SDMTools and aspace, as described in Laurent et al. (2018) (Table 1). Some of the code in these packages was slightly modified to facilitate data input/output, and to enhance performance. We also provided several additional indices at patch level to the dataset. For our results based on the FireCCI51 product, up to three most dominant land cover were indicated, with their respective percentages over the patch in terms of number of pixels. We also calculated the rate of spread (RoS), defined as the longer axis of an FP's standard deviation ellipse (SDE) divided by the duration of the fire in days (maximum BD – minimum BD + 1). Fire radiative power (FRP) data from the MODIS Collection 6 NRT Hotspot / Active Fire Detections (MCD14ML) dataset were projected to each FP/SIFP, where the mean FRP was computed following Laurent et al. (2019). Ignition location for each fire patch was also calculated as the centroid of the minimum BD clump within the patch.

Table 1: Fire patch characterization variables provided in FRYv2.

Column name	Class	Description
ptch_id	character	patch identifier
L1	integer	most common land cover type
L2	integer	second common land cover type
L3	integer	third common land cover type
LP1	numeric	% of the most common land cover type
LP2	numeric	% of the second common land cover type
LP3	numeric	% of the third common land cover type
CALCCENTRE	logical	if mean centre is calculated for the standard deviation ellipse (SDE)
Weighted	logical	if the weighted mean centre is to be used instead
CENTRE.x	numeric	x coordinate of the SDE centre [m]
CENTRE.y	numeric	y coordinate of the SDE centre [m]
Sigma.x	numeric	Half-length of axis along the shorter axis of SDE [degree]
Sigma.y	numeric	Half-length of axis along longer axis of SDE [degree]
Major	character	String indicating which axis is the major (longer) SDE axis
Minor	character	String indicating which axis is the minor (shorter) SDE axis
Theta	numeric	Angle between the longer SDE axis angle and the North, (0-180 degrees)
Eccentricity	numeric	A measure of eccentricity (i.e., the flatness of the ellipse)
Area.sde	numeric	Area of the SDE [m^2]
ThetaCorr	numeric	Corrected theta
Mindt	character	earliest BD of the patch
Maxdt	character	latest BD of the patch
n.cell	integer	number of cells
n.core.cell	integer	number of core (i.e. non-edge) cells
n.edges.perimeter	integer	number of outer perimeter cell edges of the patch
n.edges.internal	integer	number of internal cell edges of the patch.
Area	numeric	area of each patch comprising a landscape mosaic [m^2]
core.area	numeric	interior area of the patch, greater than the specified depth-of-edge distance from the perimeter [m^2]
Perimeter	numeric	perimeter of the patch, including any internal holes in the patch, specified in meters [m]
perim.area.ratio	numeric	the ratio of the patch perimeter [m] to area [m^2]
shape.index	numeric	shape complexity: sum of each patch's perimeter divided by the square root of patch area
frac.dim.index	numeric	fractal dimension index: reflects shape complexity across a range of spatial scales; approaches 2 times the logarithm of patch perimeter [m] divided by the logarithm of patch area [m^2]

Column name	Class	Description
core.area.index	numeric	quantifies core area as a percentage of patch area
Oom_sep	logical	if the patch is a result of the separation algorithm described in Oom et al. (2016)
ptch_id_Oom	character	patch identifier for the results from the separation algorithm described in Oom et al. (2016)
i.centre.x	numeric	x-coordinate of the centre of the earliest BD clump, only available for the results of the Oom et al. (2016) algorithm
i.centre.y	numeric	y-coordinate of the centre of the earliest BD clump, only available for the results of the Oom et al. (2016) algorithm
Minday	integer	earliest BD of the patch, measured as days after 31-12-2000
Maxday	integer	latest BD of the patch, measured as days after 31-12-2000
frp_mind30	numeric	mean fire radiative power, using a 30-day delay [MW]
min_frp_mind30	numeric	minimum FRP, using a 30-day delay [MW]
max_frp_mind30	numeric	maximum FRP, using a 30-day delay [MW]
sd_frp_mind30	numeric	standard deviation of FRP, using a 30-day delay [MW]
N_frp_mind30	integer	number of patches that hit a least one FRP data point, within a 30-day delay
CENTRE.LON	numeric	longitude of the patch centre [degree]
CENTRE.LAT	numeric	latitude of the patch centre [degree]
Yr	integer	year of the earliest BD
Sigma_X_m	numeric	Half-length of axis along the shorter axis of SDE [m]
Sigma_Y_m	numeric	Half-length of axis along longer axis of SDE [m]
Rsde	numeric	shorter axis / longer axis of the SDE
FSR	numeric	Fire Spreading Rate (= 2 * longer half axis / (maxday - minday + 1), [m day^{-1}]

3.1.4 Data format

FRYv2 is delivered as a set of 'csv' files of 2º by 2° tiles globally. Each file is a list of fire patches described by the list of parameters presented in Table 1. In this updated version, we also provided the yearly shapefile (SHP format) of fire contours in 2x2-degree tiles globally. Synthetic global maps were built at 0.5° and 1° resolution as yearly and monthly fire number, yearly and total (over the whole 2001-2019 period) fire size distribution slope representing the proportion of large fires compared to small fires, as well as monthly means of FRP and Shape index. Global maps are available in Geotiff format in geographic projection.

3.2 Results

3.2.1 Patch density

Fire patch numbers from FRYv1 (MCD64A1 and FireCCI41) and FRYv2 (MCD64A1 and FireCCI51) are presented in Table 2 for the 2001-2019 period, and also for the period 2005-2011, when the 2 datasets overlap. For a better comparison, we calculated for FRYv2 the fire number before and after the single-ignition separation step, and we provide the fire number obtained for a temporal threshold for pixel aggregation (cut off) of 6 and 12 days. The FRYv2 dataset detects 2.91 million FPs (before single ignition separation step) larger than 107 ha, for a BD cut-off of 6 days, i.e. 17% more the FRYv1 does, using the MCD64A1 as input, for the period of 2005-2011, probably due to the new decomposing step allowing for merged large fires to be decomposed according to potential simultaneous ignitions. The FRYv2 dataset based on FireCCI51 detected 3.60

million SIFPs larger than 107ha, or 24% more than its MCD64A1 counterpart, with the same single-ignition separation step for a 6-day cut-off and 3.26 million SIFPs for a 12-day cut-off for the 2005-2011 period. When looking at the 2001-2019 period and all fire sizes, we reached 35.5 million fires fire FRYv2 FireCCI51 with a cut-off value of 6 days and 16.52 million for a cut-off of 12 days. A lower fire number of 19.37 million was obtained for FRYv2 MCD64A1 (due to a coarser resolution and missed small fires) for a 6-day cut-off and 15.38 million fire patches for a 12-day cut-off.

Table 2: Fire patch count (in million) obtained in the FRYv1 and FRYv2 datasets. Numbers in parentheses are FP counts before the separation step to obtain single-ignition fire patches. The numbers in the second row correspond to the cut-off values.

	Period	FRYv2 FireCCI51		FRYv2 MCD64A1		FRYv1 MCD64A1		FRYv1 FireCCI41	
		6d	12d	6d	12d	5d	14d	5d	14d
>107ha	2001-2019	9.02 (7.29)	8.15 (5.74)	7.55 (6.73)	7.07 (5.89)				
	2005-2011	3.60 (2.91)	3.26 (2.30)	2.91 (2.60)	2.74 (2.28)	2.49	2.03	2.35	1.44
ALL	2001-2019	35.50 (33.30)	16.52 (13.68)	19.37 (18.24)	15.38 (13.92)				
	2005-2011	14.00 (13.12)	6.59 (5.45)	7.47 (7.08)	5.96 (5.43)	2.54	2.07	3.97	2.28

FP density global distributions are similar across input products and different BD cut-off values, and also across the FRYv1 and the FRYv2 datasets. Highest FP densities are found in African tropical savannas, Southeast Asia tropical forests, Northern Australia savannas, Brazilian Cerrado, and central Eurasia in both versions of FRY (Figure 2).

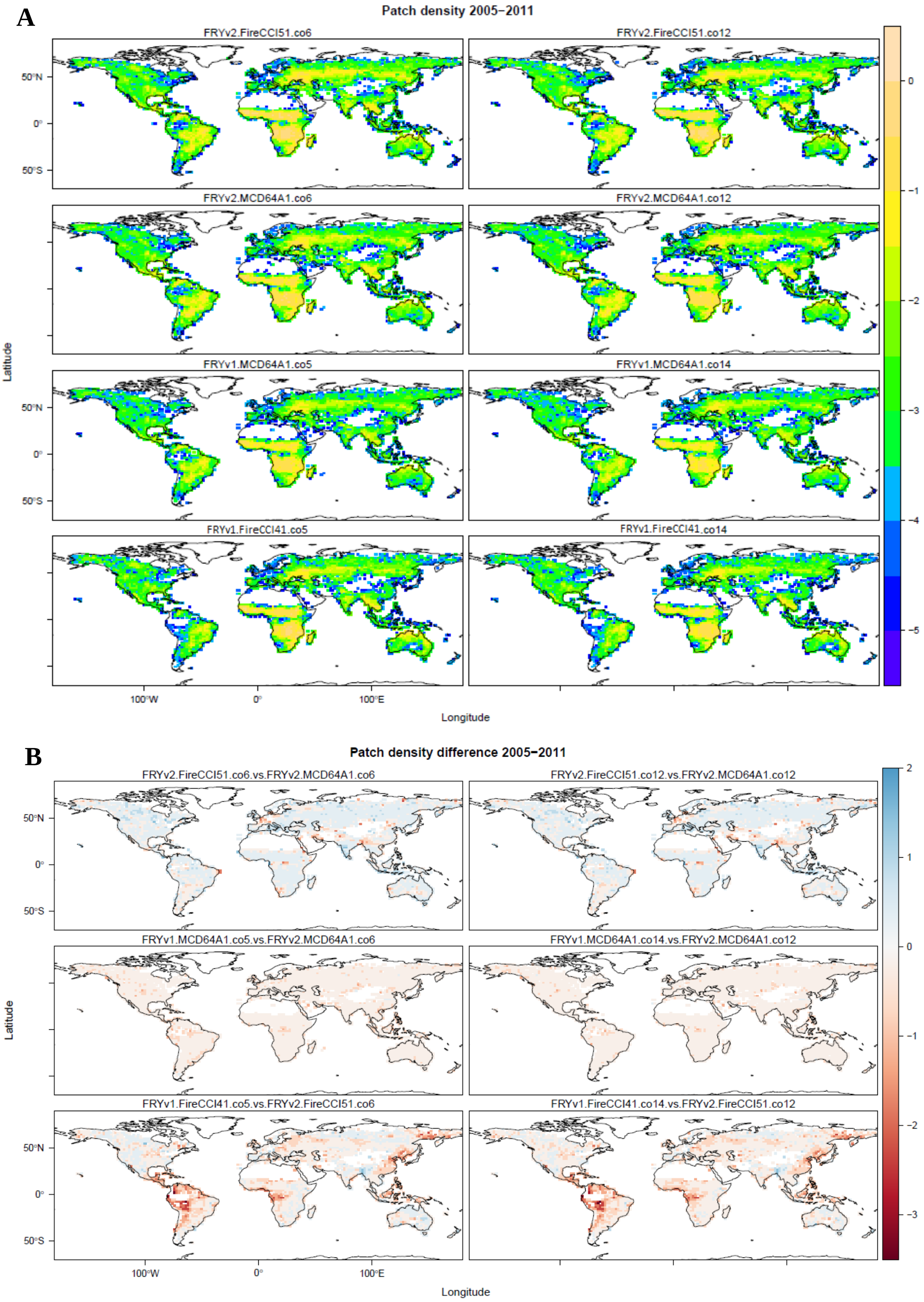

Figure 2: A) Global maps of fire patch density (log10 (number of fires).km-2) obtained for FRYv2 FireCCI51 (cut-off temporal threshold of 6 and 12 days), FRYv2 MCD6A1 (cut-off temporal threshold of 6 and 12 days), FRYv1 MCD64A1 (cut-off temporal threshold of 5 and 14 days), and FRYv1 FireCCI41 (cut-off temporal threshold of 5 and 14 days) over the 2005-2011 period. B) Global maps of fire patch density difference (in log10 (number of fires.km-2)) between FRYv2.0_FireCCI51 and FRYv2.0_MCD64A1, FRYv1.0_MCD64A1 and FRYv2.0_MCD64A1, and FRYv1.0_ FireCCI41 and FRYv2.0_ FireCCI51.

3.2.2 Fire size distribution (FSD)

The size of wildfire is acknowledged to follow a power law- or power law-like probability distribution, purportedly as a result of self-organized criticality (SOC) (Bak et al., 1988; Malamud et al., 1998; Turcotte et al., 1999). In a power law distribution, the frequency of fire is linearly related to fire size in a log-log scale, or at least towards the larger size end. Recent studies challenged the universality of SOC in wildfires by showing that fire size in some of the most fire-active regions can be equally or better described by lognormal distributions (Corral and González, 2019; Hantson et al., 2016). In Figure 3 we present the log-log plots of FSD based on the FRYv2 dataset, along with the same plots based on the previous version FRYv1. Instead of dividing the dataset according to geographical regions, we regrouped the data by biomes, following the major biome map of United states Department of Agriculture (https://www.nrcs.usda.gov/wps/portal/nrcs/detail/soils/use/worldsoils/?cid=nrcs142p2_054002). To reduce the number of groups, we further combined some similar biomes, resulting in five major biome types. Although the present dataset covers global FPs from 2001 to 2019, the comparisons below between the FRYv1 and FRYv2 datasets only cover the period of 2005-2011, since it is the range of the original FRYv1.

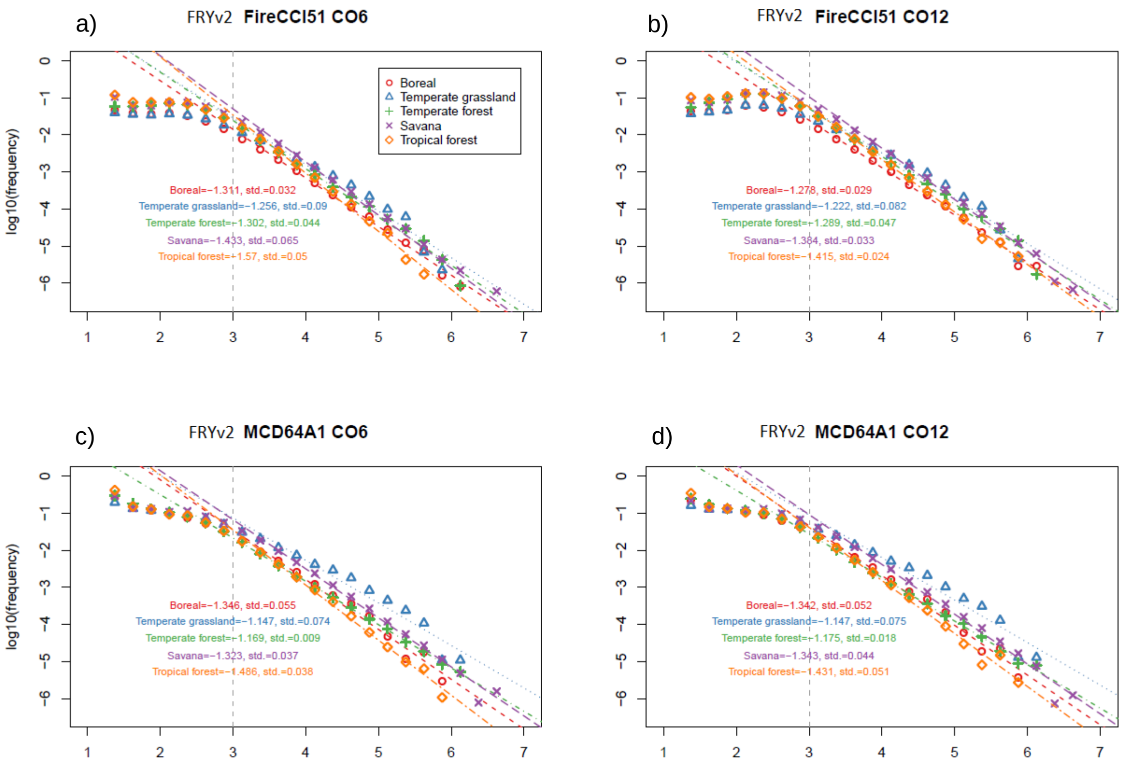

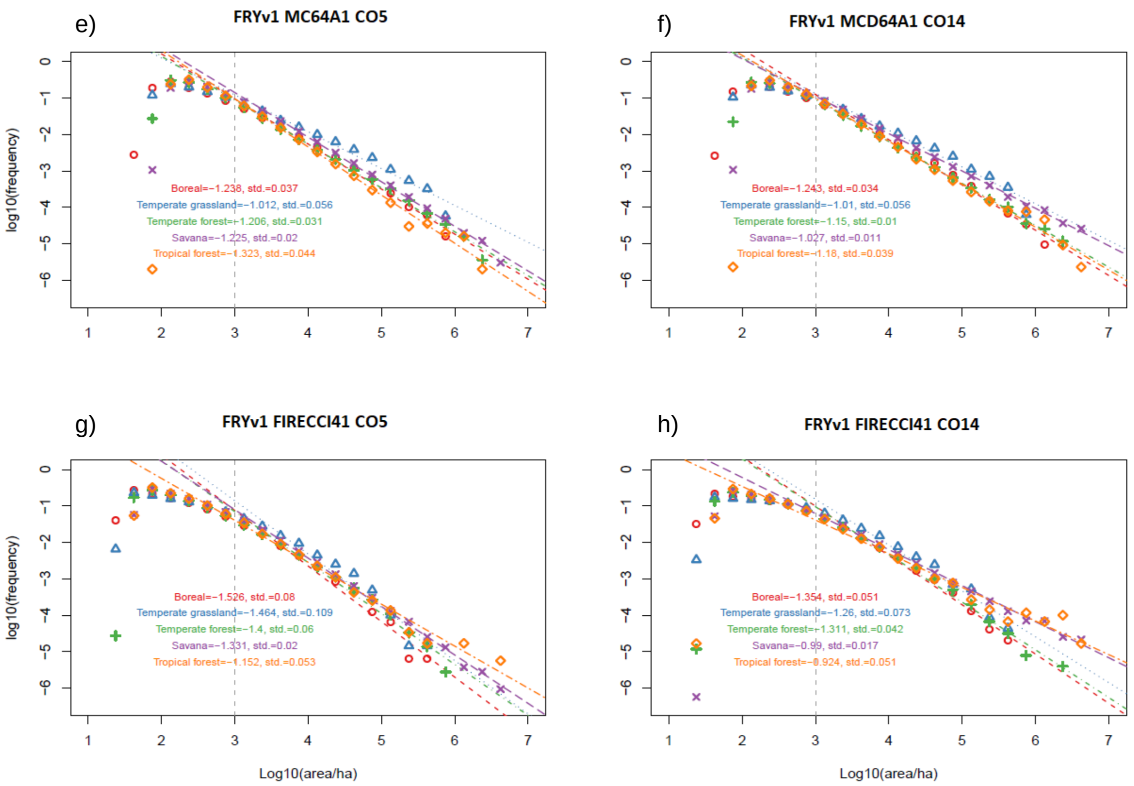

Figure 3: Fire size distribution (log/log scale) of fire patches generated from FRYv2 FireCCI51 (a-b), FRYv2 MCD64A1 (c-d), FRYv1 MCD64A1 (e-f) and FRYv1 FireCCI41 (g-h) for their two cut-off values and each biome (boreal in red, temperate grassland in blue, temperate forest in green, savannas in purple, tropical forests in brown). The slope and standard deviation of the linear regression calculated for fire size>1000ha is also presented.

The log-log plots of frequency versus fire size provide an overview of the fire patch clustering results (Figure 3). We observe that for fire sizes larger than 10^3 ha, the frequency / size relationships are approximately linear in logarithm scale for most biomes, i.e. the fire size follows a power-law distribution (Corral and González, 2019; Hantson et al. 2016). We therefore performed linear regressions for these relationships over fires of size larger than 10^3 ha, and obtained the slopes of the respective regression lines. The absolute value of the slope β is considered a measure of FSD. As a result, a FSD with a smaller β has proportionally more larger fires, compared to one with a steeper β slope (Corral and González, 2019).

In general, β values established with the data based on the FRYv2 procedure (Figure 3a-d) are larger than their counterparts with the data based on the FRYv1 procedure (Figure 3e-h). This can be explained by the extra decomposing step that separated large FPs, reducing the number of very large FPs. The same reason may also explain the fact that the differences between the β values with different BD cut-off values are much smaller in the FRYv2 results (Figure 3a-b, c-d), compared to their FRYv1 counterparts (Figure 3e-f, g-h). On the other hand, the relative magnitudes of β value across biomes remain more stable in the FRYv2 dataset than those in the FRYv1. For instance, in the FRYv2 dataset, the largest βs are found always in tropical forests, the smallest in temperate grasslands, regardless of the input product, nor the BD cut-off value. The case of the FRYv1 dataset is less stable, with some of the largest β values found in boreal biomes

(Figure 3f, g, and h) and some in tropical forests (Figure 3e), while some of the smallest β values found in temperate grassland (Figure 3e and f), others in tropical forests (Figure 3g and h). These results suggest that the FRYv2 approach is an effective way to mitigate the impact of different BD cut-off values on FSD, while keeping the characteristics of the FSD in different biomes.

When looking at the FSD for fires below 10^3 ha, we observe that FRYv2 FireCCI51 tends to prolong the linear relationship further than FRYv2 MCD64A1, suggesting a benefit for medium fire size (10^2 to 10^3 ha) characterization when using finer resolution. We also observe a significant difference between FRYv1 and FRYv2 for fire sizes lower than 10^2 ha, with very few fire patches detected in FRYv1 and no such collapse observed in FRYv2, suggesting that the single-ignition separation step might have created more small fires and better fits the SOC theoretical hypothesis.

Based on this analysis, we provide the fire size distribution global (1° resolution) maps for fire size >1000 ha in Figure 4, for the newly delivered FRYv2.0.FireCCI51 (cut off 6 and 12 days). For comparison, we also provide the same global fire size distribution map for FRYv2.0.MCD64A1, FRYv1.0.MCD64A1, and FRYv1.0.FireCCI41, as well the difference maps. The regression slope is mostly steeper for FRYv2.0.FireCCI51 than FRYv2.0.MCD54A1 as a result of more frequent smaller fires detected, expected in India and Central Asia. No major differences in FSD were observed between the two pixel-aggregation methods for the same sensor MCD64A1, suggesting a bigger effect of pixel resolution than the aggregation method in the differences between FRYv2.0 and FRYv1.0.

A

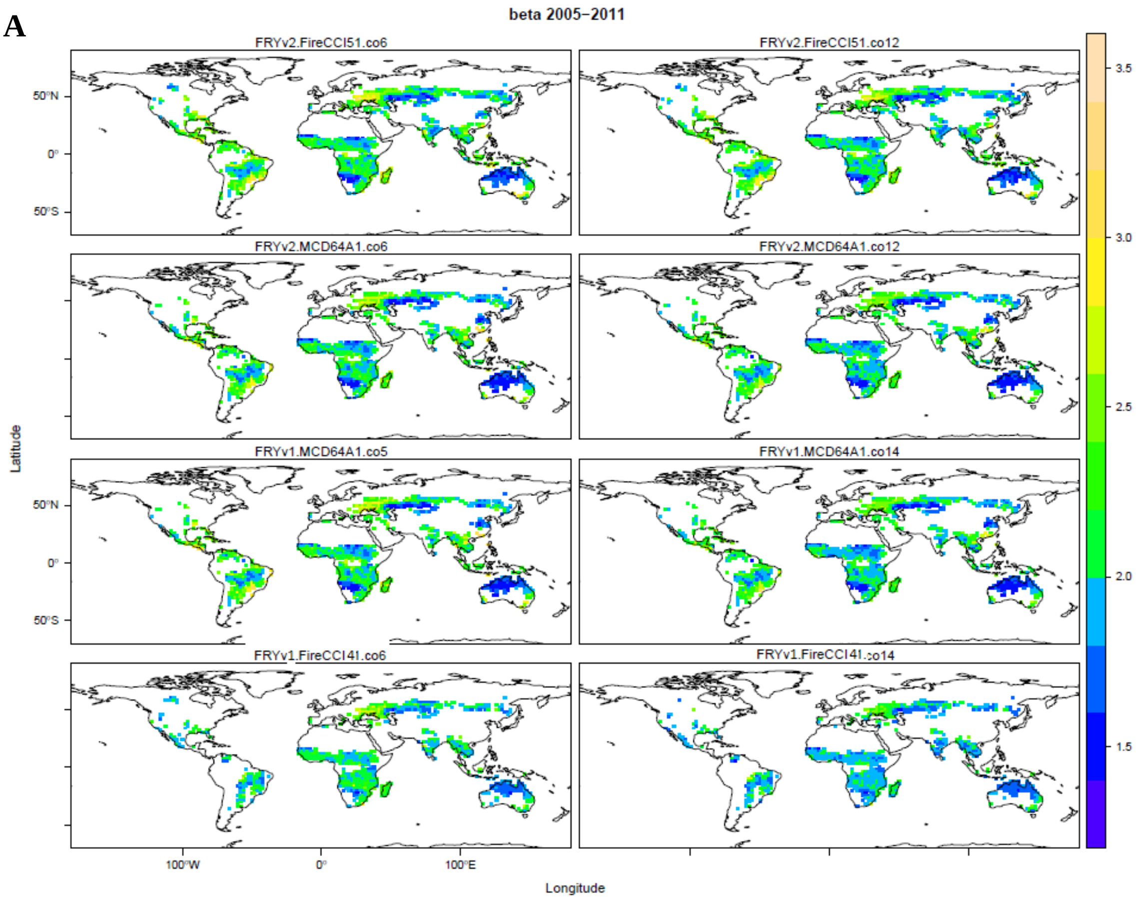

B

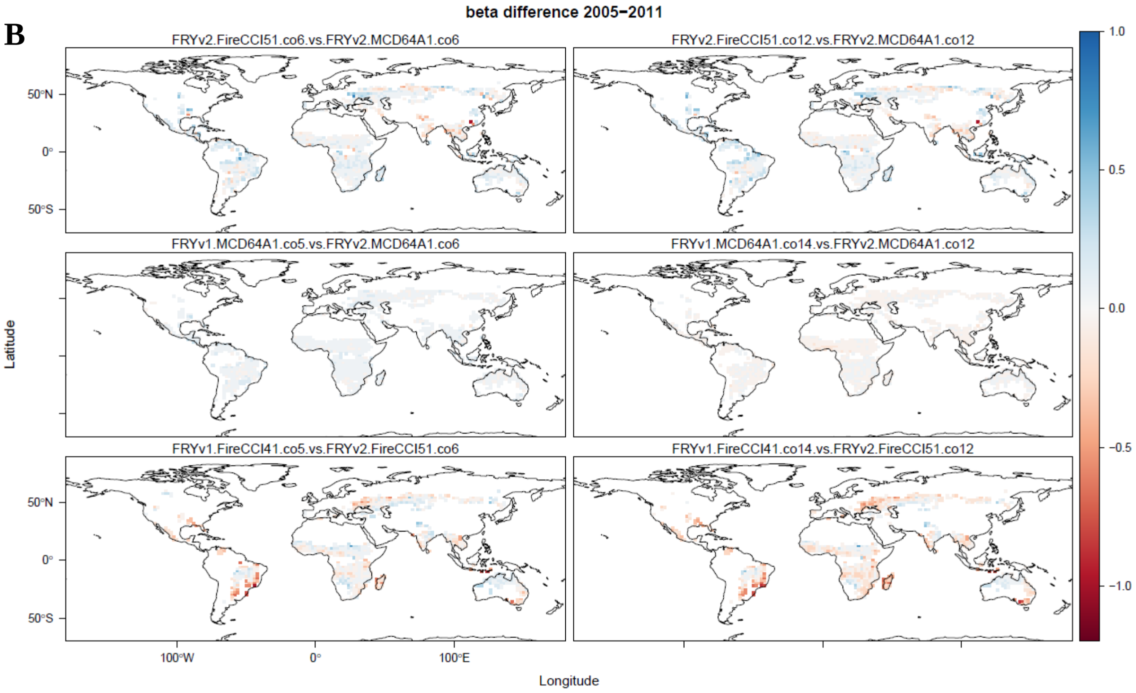

Figure 4: A) Global maps of fire size distribution slopes for fires>1000ha for FRYv2.0.FireCCI51, FRYv2.0.MCD64A1, FRYv1.0.MCD64A1 and FRYv1.FireCCI41 for temporal cut-off values of 6 days (left) and 12 days (right). B) Global difference maps between FRYv2.0.FireCCI51 and FRYv2.0.MCD64A1, FRYv1.0.MCD64A1 and FRYv2.0.MCD64A1, and FRYv1.0.FireCCI41 and FRYv2.0.FireCCI51.

3.2.3 Shape index (S.I.)

Shape indices based on the MCD64A1 product are similar in both FRYv1 and FRYv2, with slightly higher values in the FRYv1 results (Figure 5, Figure 6). Since the FRYv1 results have larger BD cut-off than the FRYv2 ones do (5d versus 6d), the smaller S.I. found in the FRYv2 dataset may be a result of the FP separation process. On the other hand, both the results based on the FireCCI41 product in FRYv1, and those based on FireCCI51 in FRYv2 have systematically larger S.I. than those of their MCD64A1 counterparts, by around 70% in median value (Laurent et al., 2018). The higher S.I., indicting higher patch complexity in those datasets, can be explained by the higher spatial resolution in the FireCCI41 (300m) and in the FireCCI51 (250m) compared to MCD64A1 (500m), as a result of ‘stair-step’ aliasing of BD pixels (Laurent et al., 2018). Furthermore, higher S.I. may also be to the ‘growing’ phase in both the FireCCI41 and FireCCI51 algorithms enabling the reconstruction of larger fire patches. Regardless of the systematic differences in S.I. across different datasets, it is possible to distinguish regions of higher fire complexity from those with a lower one. Indeed, relatively high S.I. are found in boreal and temperate regions in the Northern Hemisphere, still biased with latitude because of the geographic projection.

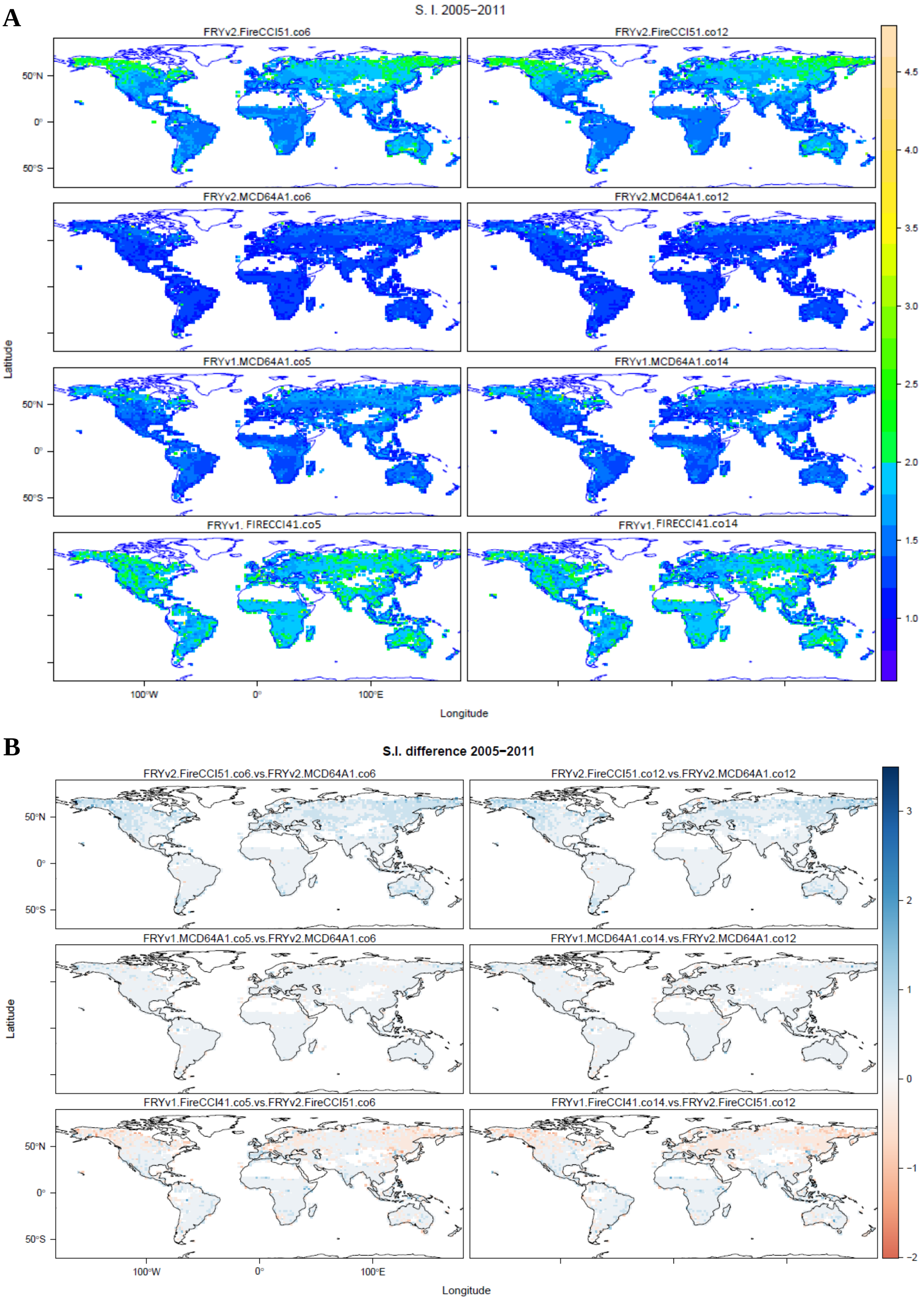

Figure 5: A) Global maps of mean shape index (S.I.) for the period 2005-2011 for fire patches from FRYv2 FireCCI51 (cut-off temporal threshold of 6 and 12 days), FRYv2 MCD64A1 (cut-off temporal threshold of 6 and 12 days), FRYv1 MCD64A1 (cut-off temporal threshold of 5 and 14 days) and FRYv1 FireCCI41 (cut-off temporal threshold of 5 and 14 days). B) Global difference maps between FRYv2.0.FireCCI51 and FRYv2.0.MCD64A1, FRYv1.0.MCD64A1 and FRYv2.0.MCD64A1, and FRYv1.0.FireCCI41 and FRYv2.0.FireCCI51.

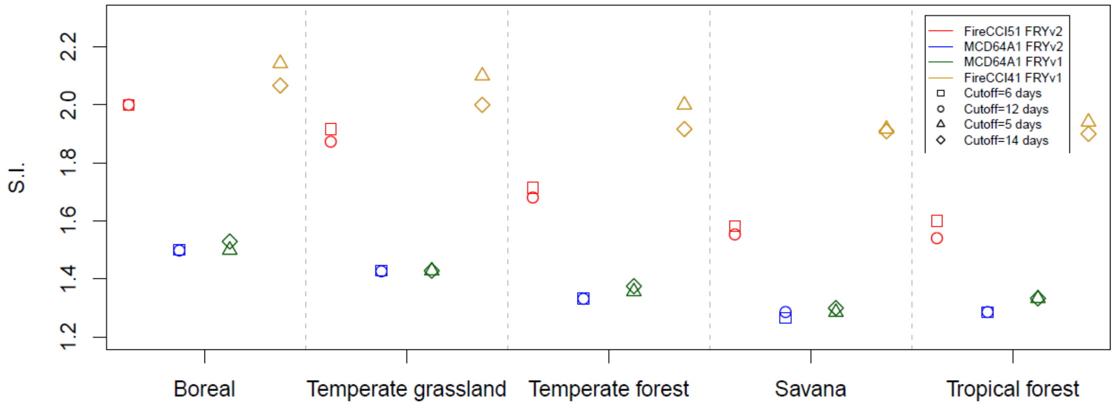

Figure 6: Mean shape index (S.I.) per fire patch for each biome (Boreal, Temperate grasslands, temperate forests, savannas and tropical forests) and for each dataset FRYv2 FireCCI51 (red), FRYv2 MCD64A1 (blue), FRYv1 MCD64A1 (green) and FRYv1 FireCCI41 (brown).

3.2.4. Standard deviation ellipse ratio (Rsde) and Fire duration

Further analysis of two of the functional traits, R_{sde} and fire duration are presented in Figure 7 and Figure 8, respectively. R_{sde} (Figure 7) is the ratio between the length of shorter axis and that of the longer axis on the fire patch's SDE, so that lower values indicate more elongated fire patches. It measures the relative elongation of the FP. In general, the FRYv2 method produced slightly less elongated FPs than the FRYv1 did (higher R_{sde}), especially in biomes of higher latitudes (boreal forests and temperate grasslands). However, the range of variation between different methods and among input products is small, with the median ranging from 0.54 in the FRYv1 FireCCI41 savannas, to 0.61 in the FRYv2 MCD64A1 boreal forests. Besides, the effect of BD cut-off value is not detectable in the FRYv2 datasets.

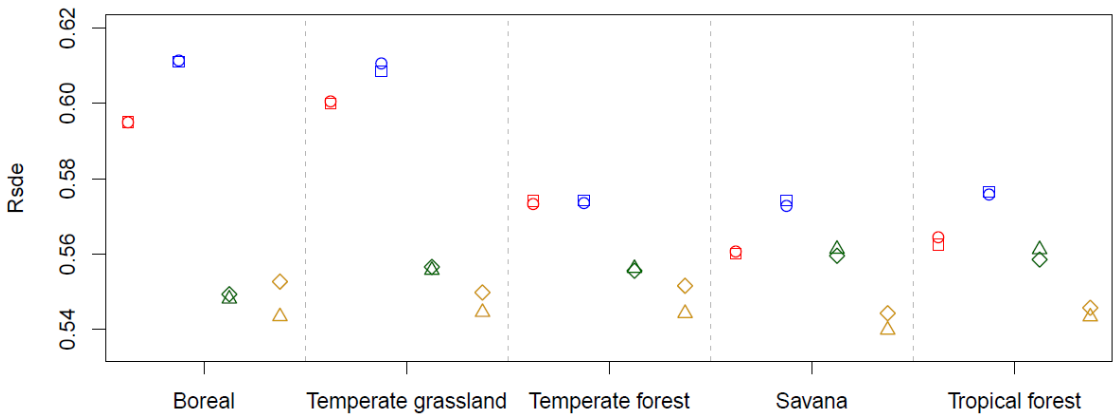

Figure 7: Mean ratio of ellipse axis (shorter axis/longer axis) per fire patch for each biome (Boreal, Temperate grasslands, temperate forests, savannas and tropical forests) and for each dataset FRYv2 FireCCI51 (red), FRYv2 MCD64A1 (blue), FRYv1 MCD64A1 (green) and FRYv1 FIRECCI41 (brown). Temporal cut-off thresholds for pixel aggregation are 6 days (square), 12 days (circle), 5 days (triangle) or 14 days (diamond).

Fire duration (Figure 8) was measured as the difference of the latest and earliest BD values of a FP in days, plus one to avoid zero difference. Longer BD cut-off values produced FPs with longer durations across all datasets, as expected. The FRYv2 FireCCI51 dataset yielded the longest median durations across most biomes, especially with a cut-off value of 12 days. FRYv1 and v2 based on MCD64A1 have very close median durations, while the v2 dataset, compared to that of v1, has longer duration with a 6-day cut-off, and at higher latitudes. The temporal resolution difference between the FireCCI51 (one-day) and the FireCCI41 (3-day) may explain the large difference in fire duration, since a large amount of FPs would have been detected at the same date, even though they actually have persisted for two or three days, which is the temporal resolution of the ENVISAT-MERIS sensor used in FireCCI41.

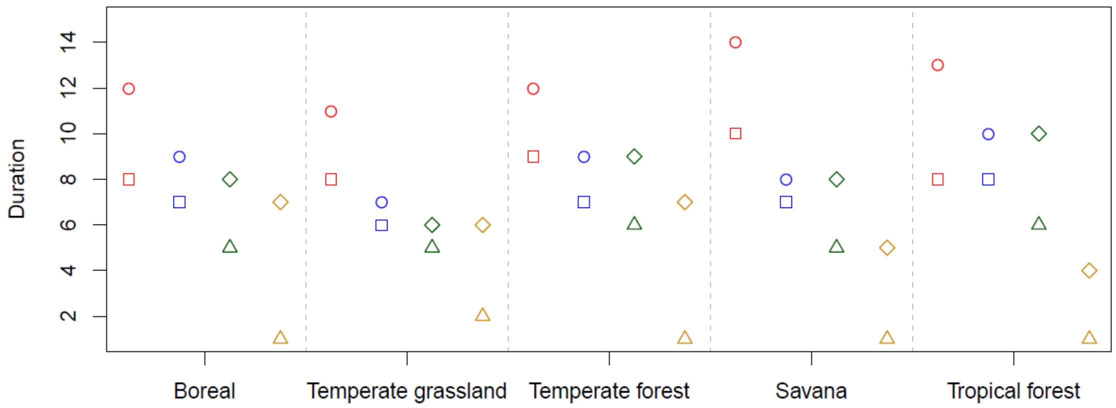

Figure 8: : Mean fire duration (in days) per fire patch for each biome (Boreal, Temperate grasslands, temperate forests, savannas and tropical forests) and for each dataset FRYv2 FireCCI51 (red), FRYv2 MCD64A1 (blue), FRYv1 MCD64A1 (green) and FRYv1 FireCCI41 (brown). Temporal cut-off thresholds for pixel aggregation are 6 days (square), 12 days (circle), 5 days (triangle) or 14 days (diamond).

3.2.5 FRP mapping

Among the FPs larger than 107ha in the FRYv2 FireCCI51 dataset, over 95% were matched to at least one FRP points (Table 3). The match rates for FPs in the FRYv2 MCD64A1 dataset are lower to ca. 74%. The FRYv1 datasets have intermediate match rates of ca. 85%. Median value of patch-averaged FRP is constant around 24 MW in the FRYv2 FireCCI51 dataset across biomes (Figure 9). In the other datasets (two MCD64A1s, and FireCCI41), however, this value is substantially higher in higher-latitude biomes (boreal and temperate grasslands) than in biomes of lower latitude. This difference can be explained by a larger number of FPs of size between 100 to 1000 ha that were detected in the FRYv2 FireCCI51 dataset in those biomes of higher latitude. It also suggests that most of these FPs are related to relatively lower FRPs, and therefore demonstrates an advantage of the FireCCI51 dataset in detecting lower-intensity fires.

Table 3: Ratio of fire patches matched to at least one FRP data point across datasets

Dataset	Cut-off (days)	FRP match ratio
FRYv2 FireCCI51	6	0.952
FRYv2 FireCCI51	12	0.967
FRYv2 MCD64A1	6	0.735

FRYv2 MCD64A1	12	0.748
FRYv1 MCD64A1	14	0.831
FRYv1 FireCCI41	14	0.874

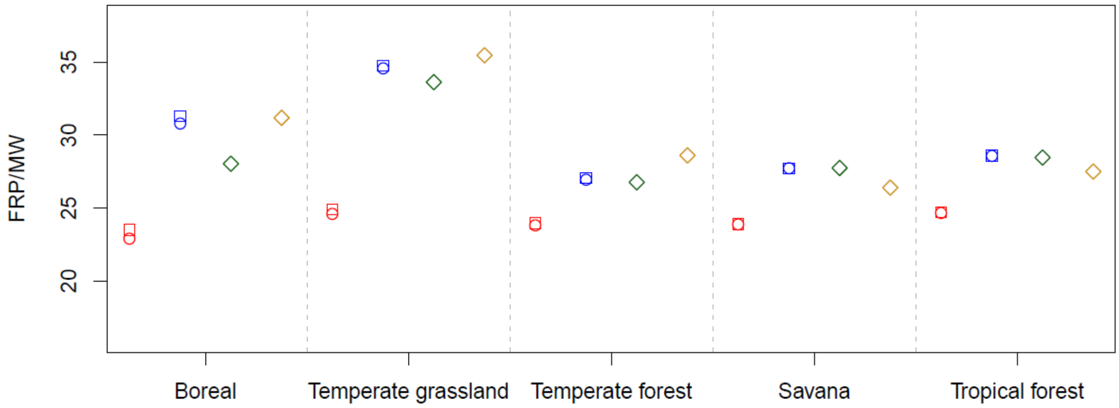

Figure 9: Mean Fire radiative power (FRP, in MW) per fire patch for each biome (Boreal, Temperate grasslands, temperate forests, savannas and tropical forests) and for each dataset FRYv2 FireCCI51 (red), FRYv2 MCD64A1 (blue), FRYv1 MCD64A1 (green) and FRYv1 FireCCI41 (brown). Temporal cut-off thresholds for pixel aggregation are 6 days (square), 12 days (circle), 5 days (triangle) or 14 days (diamond).

4. FRY_SFD: fire patch database for Africa 2019 from FireCCISFD20

4.1 Material and Method

The Small Fire Dataset v2.0 (FireCCISFD20) is a product derived from the remote-sensing images of two Copernicus Sentinel-2 satellites. It covers Sub-Saharan Africa for the year 2019. The product provides burned area detection at 20m resolution every 5-10 days. The dataset is distributed in 5×5-degree non-overlapping tiles (Pettinari and Roteta, 2021).

The FireCCISFD20 PIXEL product was used in preparing the FRY_SFD dataset. This PIXEL product contains a very large amount of high-resolution spatial data in pixels, compared to its FireCCI51 and MCD64A1 counterparts. Therefore, we modified the pixel-aggregation and Oom-separation algorithms, in order to keep the computation time compatible with a desktop PC. First, we divided the whole 2019 dataset into three consecutive periods: from January to April, from May to September, and then from October to December. Supposing there is no more than one fire in each pixel within each period, we combined all the monthly raster data within each period into a single raster map. We then cut each resulting 5×5-degree tiles into 100 0.5×0.5-degree non-overlapping sub-tiles, similar to the respective procedures for the FireCCI51 and the MCD64A1 datasets. Subsequently, we aggregated the pixels in each sub-tile according to their BDs, grouping neighbouring pixels (queen-scheme) sharing the same BD into one cluster. Each resulting cluster had therefore one single BD. These clusters themselves were then aggregated according to neighbouring relationships and to the difference of BDs with a 6-day cut-off (12-day cut-off was not applied). We then aggregated the resulted multi-BD clusters in neighbouring sub-tiles and/or consecutive periods, according to the same 6-day cut-off. The Oom-separation algorithm performed on the FPs resulted from the previous step was identical to its FireCCI51, and MCD64A1 counterparts, except that instead of smoothing the BDs before separation, we converted, if possible, the BD of all the single-BD clusters smaller than 50 pixels to that of its largest neighbouring single-BD cluster. This procedure allowed us to avoid over-fragmenting the FPs while limiting the amount of computation. The separated FPs were used as the final output.

4.2 Results

4.2.1 Fire patch density

Using the fine resolution FireCCISFD20 pixel-level dataset induced a much higher fire number from 572,870 fires patches obtained for MCD64A1 to 1,083,220 fires for FireCCI51 and 126,118,573 for FireCCISFD20. The fire density map (Figure 10) illustrates how, despite a higher fire number generated with FireCCISFD20, the spatial pattern of fire density is conserved across sensors. When looking at fires >100ha, i.e. omitting all very small fires, FireCCI51 (310,223 FPs) and FireCCISFD20 (608,321 FPs) still generated more fires patches than MCD64A1 (242,491 FPs), with 27,9% and 151% increase, respectively, suggesting that increasing the spatial resolution of sensors not only allow for small fire detection but also allow to prevent patch aggregation into artificial large fires.

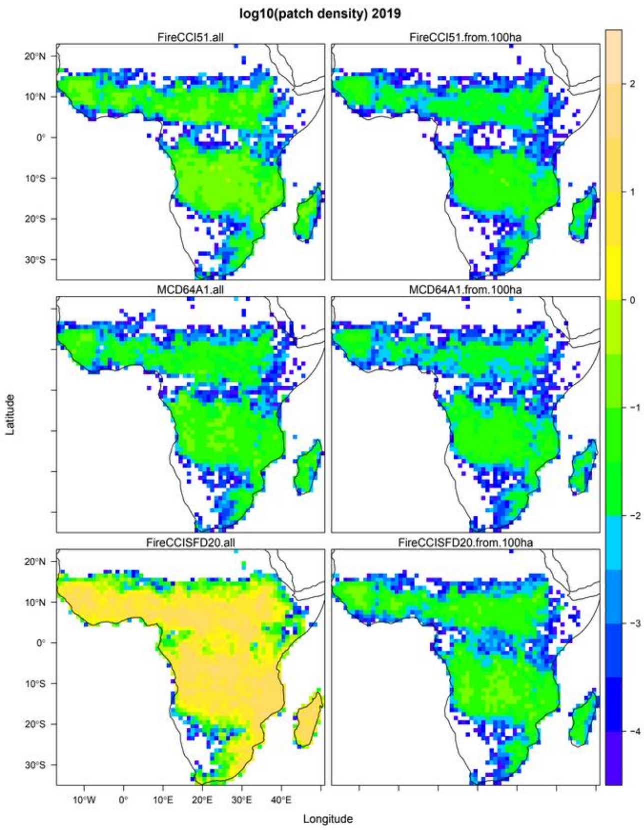

Figure 10: Maps of fire patch density (number of fires per km²) generated from pixel-level information for FireCCI51, MCD64A1 and FireCCI SFD20. Fire patch density for all fires (left panels) and fires larger than 100ha (right panel) are presented.

4.2.2 Fire size distribution

The slope of the fire size distribution (log/log scale) illustrates the proportion of large fires when compared to smaller ones. A steeper slope (higher β value) indicates more small fires than lower beta values. We observe a fair agreement between MCD64A1 and FireCCI51 with slightly steeper slopes for FireCCI51 (Figure 11) for fires>100ha (10^6m2), and suggesting more small fires frequency than large fires in this latter dataset. The slope of the fire size distribution for SFD20 is steeper than both FIRECCI and MCD54A1 all over the African continent. This result supports our previous conclusion based on patch density, that increasing sensors spatial resolution might then prevent artificial pixel aggregation into large fire size (>1000ha), and can generate more numerous smaller fires. When using a 1ha threshold (10^4m2) with FireCCISFD20, a lower slope was obtained suggesting that omitting small fires in FireCCI51 and MCD64A1 deviates the actual slope of the fire size distribution.

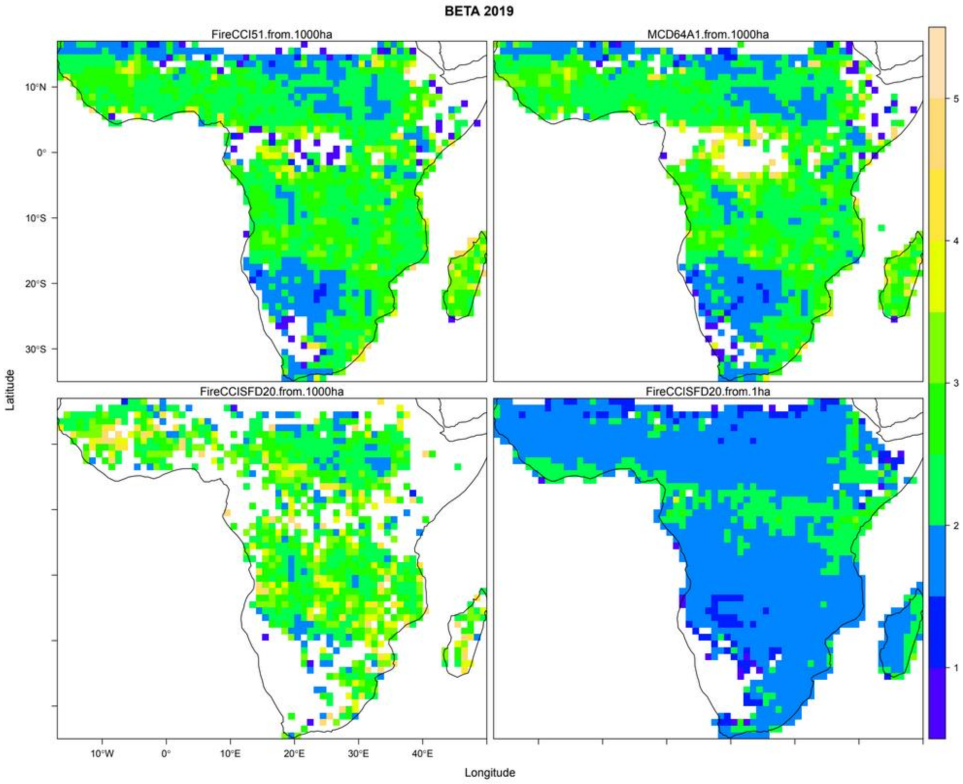

Figure 11: Maps of slope of the fire size distribution curves (β) obtained for fire patches generated from pixel-level information from FireCCI51, MCD64A1 and FireCCISFD20. A 1000ha threshold was applied for all datasets. For FireCCISFD20, a 1ha threshold was also applied (bottom right panel).

When looking at the fire size distribution curves (Figure 12) for savannas, we confirm the close relationship between MCD64A1 and FireCCI51 with increasing fire patch detection when going lower than 10^5m2 (10ha) for FireCCI51, but still omitting some fires between 10^5 and 10^6.5 m^2. When comparing to FireCCISFD20, we confirm our previous hypothesis that the break in the linear relationship obtained for FireCCI51 and MCD64A1 below 200ha (10^6.2 m^2 = 160ha) is artificial as the linear relationship is extended back to $10^{3.5}$ m^2 (0.3 ha) with FireCCISFD20. We conclude that the β value of the FSD has to be carefully built above the threshold of 200ha. For FireCCISFD20, the fire size distribution follows a linear relationship down to $10^{3.5}$ m^2 (0.3ha), highly increasing the reliability of the dataset according to the self-organized criticality (SOC) hypothesis.

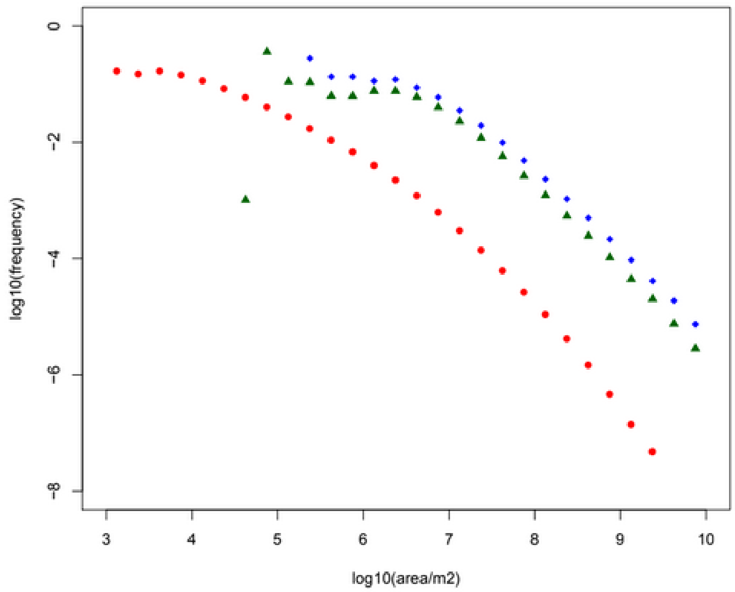

Figure 12: Fire size distribution curves obtained for the year 2019 in the the savanna biome of Africa based on fire patches obtained from pixel-level information from MCD64A1 (blue dots), FireCCI51 (green dots) and FireCCISFD20 (red dots).

4.2.3. Fire patch morphology: Shape index

The shape index assesses the complexity of the fire patch boundary, with increasing values indicating more complex fire contours. Figure 13 illustrates the mean S.I. for all fires over Africa and for fires >100ha. Considering “all fires” includes all small fires with lower boundary complexity compared to their size and pixel resolution, so that a weak difference is observed between sensors. When homogenising datasets for fires >100ha, we obtained a mean fire S.I. much higher for FireCCI51SF20 and FireCCI51 compared to MCD64A1, by 6 and 2 times respectively. This result highlights the benefits of increasing pixel resolution on fire boundary detection

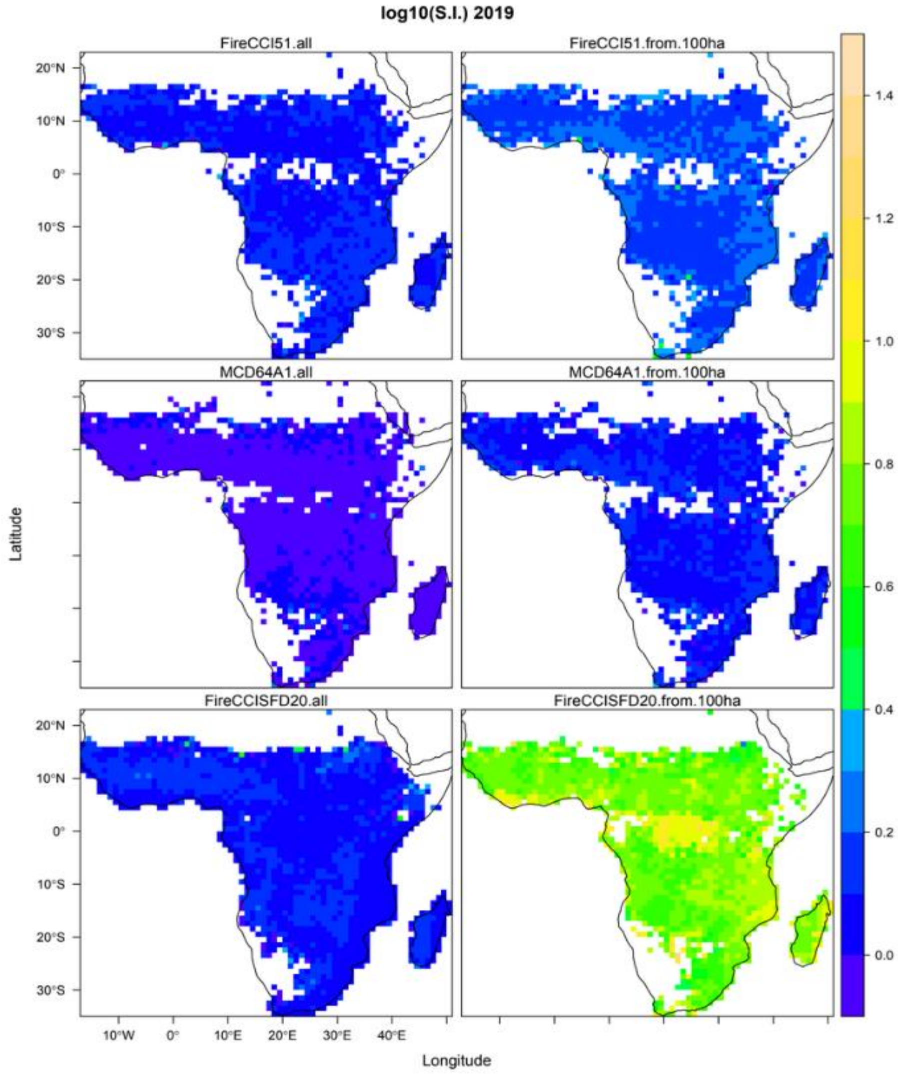

Figure 13: Mean shape index (S.I.) for each sensors FireCCI51, MCD64A1 and FireCCISFD20 when considering all fires (left panels) and fires larger than 100ha (right panel).

5. Fire Patch applications for fire modelling

Fire patches generated from pixel-level information provide a new set of information for fire modelling in biosphere/atmosphere interactions. Regarding the potential discrepancies between burned area and global carbon emissions (Zheng et al. 2022), and the recent interest in Mega fires (Godfree et al. 2021) we tested here if there is a correlation between high burning years and large fire events, or a decoupling between total burned area and number of large fires. It is mostly acknowledged that high burning years are driven by extreme large fire events, but this hypothesis has not been fully investigated globally. To test this hypothesis, we constructed the yearly maps of fire size distribution from the FRYv2 based on the FireCCI51 pixel-level information for the period 2003-2019. Even though the FireCCI51 data are available since 2001, FireCCI51 is less reliable for the years 2001-2002 as the active fire information driving the burned area algorithm was available only from the Terra satellite, while since mid-2002 both Terra and Aqua active fires were available and used in the algorithm. We normalized the β slope and the yearly burned area, so we could generate for each 1-degree tile the yearly anomaly in both burned area and the slope of the fire size distribution. Figure 14 illustrates the tile to tile relationship between the normalised β and burned area anomalies. For most of the tiles, positive anomalies in burned area correspond to a negative anomaly in the slope of the fire size distribution, illustrating that high fire years are driven by larger fires (red square). On the contrary, negative anomalies in yearly burned area correspond to positive anomalies in the slope of the fire distribution, illustrating that low fire years are composed of more dominant small fires (blue square). However, for some tiles and years, low burning years can correspond to years with large fires (green square), or high burning years can correspond to years with dominant small fires (orange square), mitigating our acknowledged hypothesis.

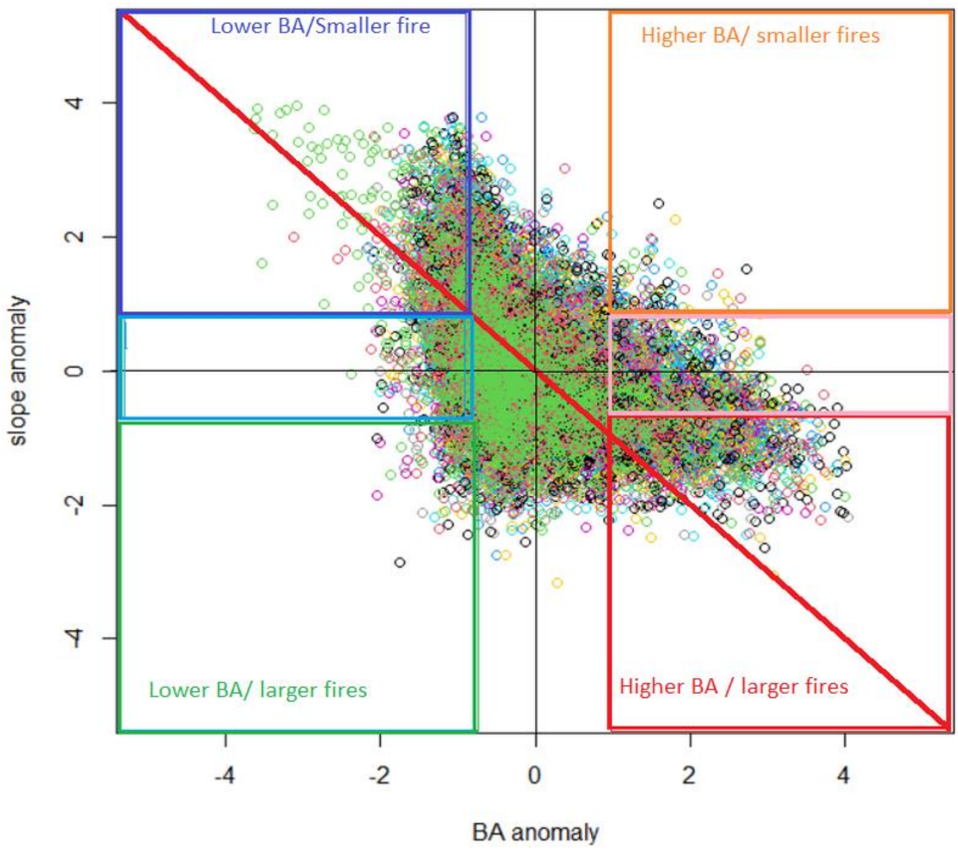

Figure 14: Relationship between annual burned area anomalies (X Axis) and slope anomalies in the annual fire size distribution for years 2003 to 2019. Squares (red, blue, green, orange, cyan and pink) represent combined anomaly types further used in Figure 13.

We plotted in Figure 15 the yearly global maps of combined anomalies in burned area and fire size distribution according to the colour code generated in Figure 14. Expected anomalies (blue and red) are mostly dominant in the temperate and boreal biomes, with high-fire years leading to large fires (red) observed in Alaska (2004 and 2009), far East Russia (2008, 2012) or Eastern USA (2017, 2018), and low-fire years dominated by smaller fires (blue) observed in Australia (2003, 2005, 2008) or far East Russia (2004). In Africa, extreme events in total burned and fire size are mostly not significant, and some years with lower total burned area associated to larger fires (green) are observed for years 2004, 2005 and 2018. This result illustrates how specific processes might happen so that low burning years can be still composed of large fires and might deserve attention in global fire models.

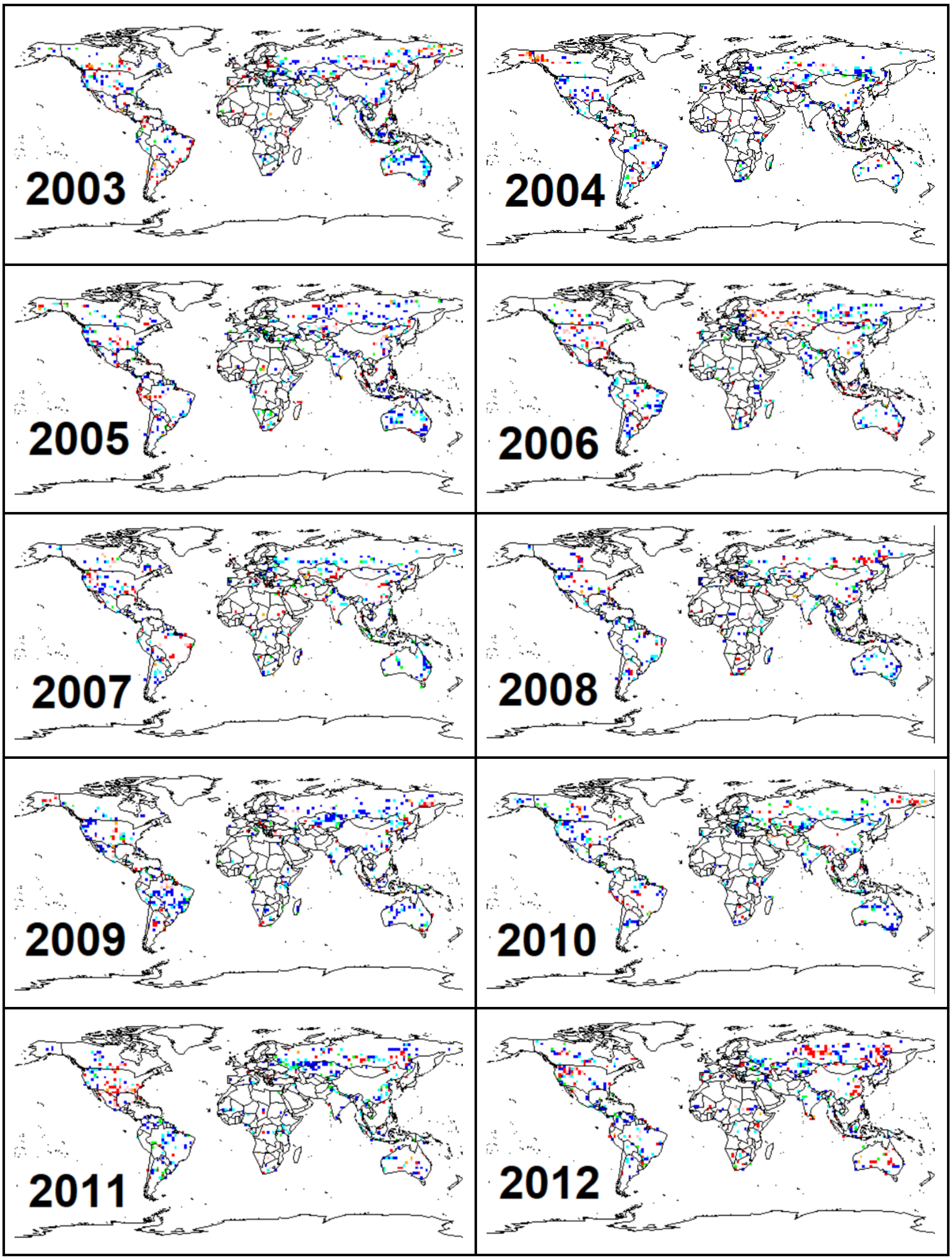

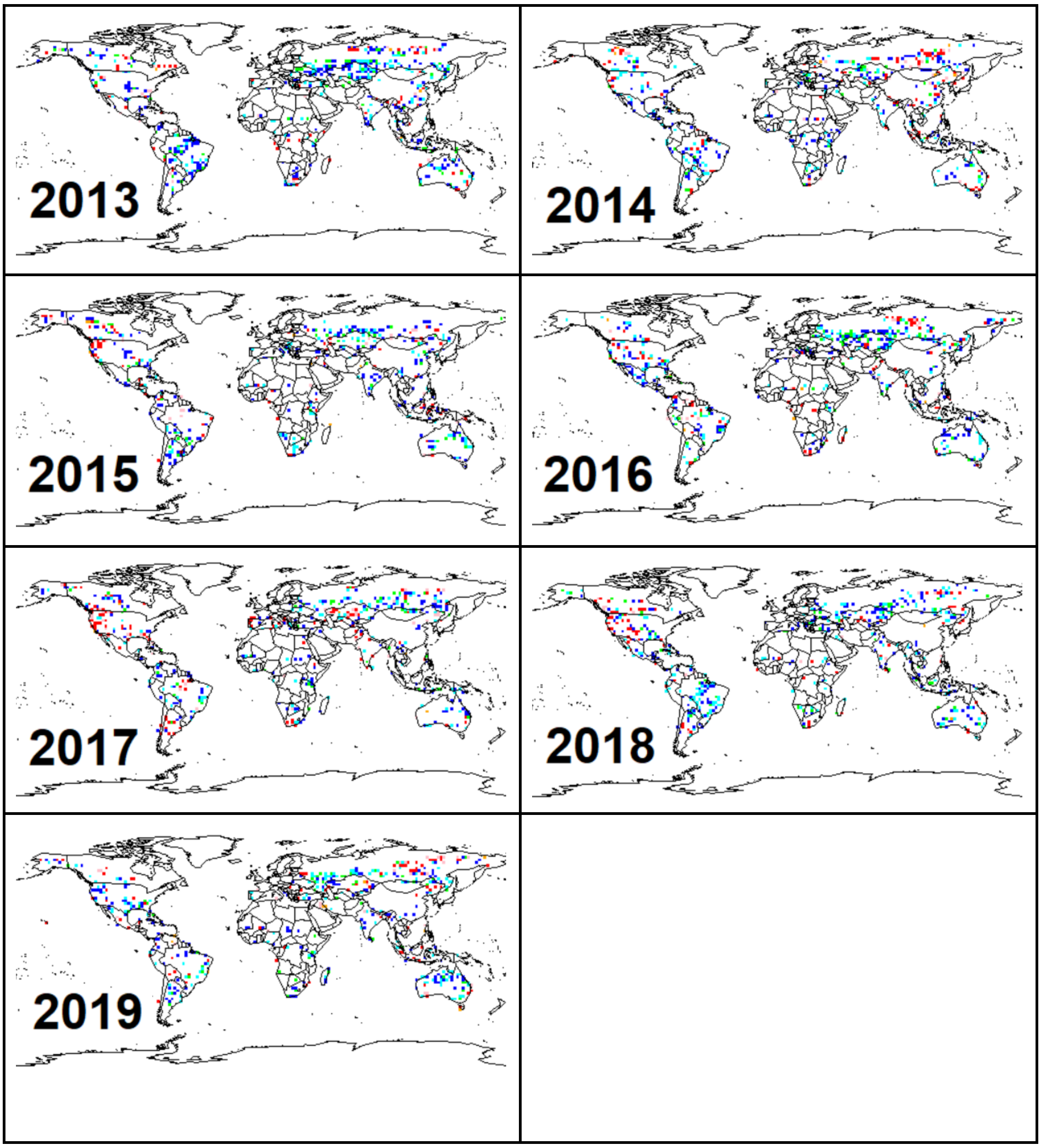

Figure 15: Yearly maps of combined anomaly types (Figure 14). Red: high burning years with lower fire size distribution slopes indicating numerous large fires. Blue: low burning years with steep fire size distribution slopes indicating few large fires. Green: low burning years with lower fire size distribution slopes indicating numerous large fires. Orange: high burning years with dominant small fires. Cyan and pink represent respectively low burning years and high burning years with no extreme fire size distribution slopes.

When looking at the temporal trend in combined anomalies occurrence across the globe (Figure 16), we observe no trends in positive and negative combined anomalies (red and blue respectively). The lower burned area combined with larger or regular fire size events anomaly types (green and cyan respectively) tend to increase, suggesting that larger-fires frequency tend to increase without increasing the total burned area, a new features in global fire trend that should get further attention in fire emission modelling relying only on burned area.

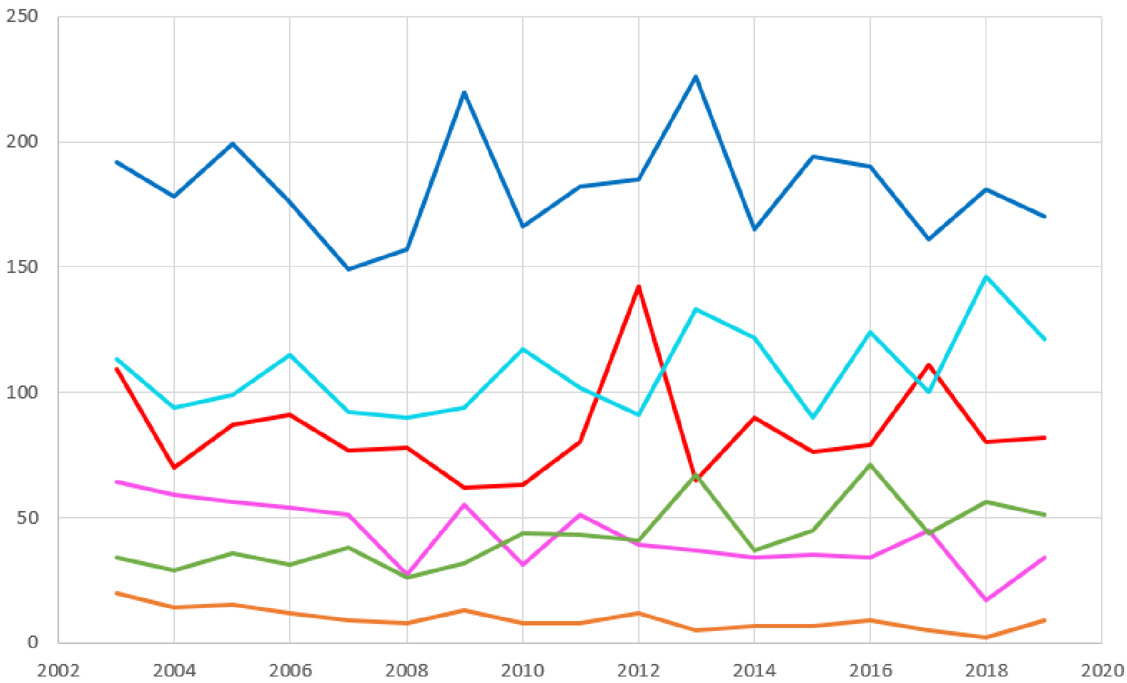

Figure 16: Temporal trend in combined anomalies occurrence across the globe. Red: high burning years with lower fire size distribution slopes indicating numerous large fires. Blue: low burning years with steep fire size distribution slopes indicating few large fires. Green: low burning years with lower fire size distribution slopes indicating numerous large fires. Orange: high burning years with dominant small fires. Cyan and pink represent respectively low burning years and high burning years with no extreme fire size distribution slopes.

6. Conclusions

We assessed the benefits of the increasing spatial resolution of both FireCCI51 and FireCCISFD20 for generating fire patches as a keystone dataset for fire emission calculations and global fire model benchmarking.

- We generated the global fire patch morphology database FRYv2, as a significant update of FRYv1 regarding the number of information in the fire patch characterisation and the finer spatial resolution of the pixel-level information. New information on fire spread and ignition points have been delivered according to user feedbacks and requirements.
- The new algorithm allows for isolating fire patches ignited simultaneously and merging into one single fire, in turn reducing the frequency of very large fires.
- Comparison of the FRYv2 with FRYv1 illustrated benefits of the finer resolution in the fire size distribution and the number of fire patches detected, as well as the complexity of fire boundaries. Large fire patches features have been conserved between MCD64A1 and FireCCI51 but increasing information is delivered with FireCCI51.
- The small fire dataset FireCCISFD20 delivered for Africa for the year 2019 at 20m resolution was tested for generating fire patches. The pixel aggregation method was successfully updated to fasten the processing of this huge dataset by analysing the external fire patch pixels rather than the whole fire patch. The fire size distribution analysis revealed the artificial distribution observed below a fire size threshold of 200ha for FireCCI51 and MCD64A1. Fire patch distribution

followed the self-organized criticality distribution down to a fire size threshold of 0.5ha, highly improving our understanding of small fires dynamic in Africa and providing 100 times more fires than coarse resolution datasets.

FRYv2 was quality checked and is available for further use by the climate scientific community, currently on request, and soon as part of the CEDA archive.

7. References

Andela, N., Morton, D. C., Giglio, L., Paugam, R., Chen, Y., Hantson, S., van der Werf, G. R., Randerson, J. T. (2019) The Global Fire Atlas of individual fire size, duration, speed and direction, Earth Syst. Sci. Data, 11(2), 529–552, doi:10.5194/essd-11-529-2019.

Bak, P., Tang, C., Wiesenfeld, K. (1988) Self-organized criticality, Phys. Rev. A 38, 364–374.

Chuvieco, E., Lucrecia Pettinari, M., Lizundia-Loiola, J., Storm, T., Padilla, M. (2018). ESA Fire Climate Change Initiative (Fire_cci): MODIS Fire_cci Burned Area Pixel product, version 5.1. Centre for Environmental Data Analysis, https://doi.org/10.5285/58f00d8814064b79a0c49662ad3af537

Corral, Á., González, Á. (2019). Power Law Size Distributions in Geoscience Revisited. Earth and Space Science, 6(5), 673–697. https://doi.org/10.1029/2018EA000479

Giglio, L., Schroeder, W., Justice, C. O. (2016). The collection 6 MODIS active fire detection algorithm and fire products. Remote Sensing of Environment, 178, 31–41, https://doi.org/10.1016/j.rse.2016.02.054

Godfree, R.C., Knerr, N., Encinas-Viso, F. *et al.* (2021) Implications of the 2019–2020 megafires for the biogeography and conservation of Australian vegetation. *Nat Commun* **12,** 1023. https://doi.org/10.1038/s41467-021-21266-5

Hantson, S., Pueyo, S., Chuvieco, E. (2016). Global fire size distribution: From power law to log-normal. International Journal of Wildland Fire, 25(4), 403–412, https://doi.org/10.1071/WF15108

Laurent, P., Mouillot, F., Vanesa Moreno, M., Yue, C., & Ciais, P. (2019). Varying relationships between fire radiative power and fire size at a global scale. *Biogeosciences*, *16*(2), 275–288. https://doi.org/10.5194/bg-16-275-2019

Laurent, P., Mouillot, F., Yue, C., Ciais, P., Moreno, M. V., Nogueira, J. M. P. (2018). Data Descriptor: FRY, a global database of fire patch functional traits derived from space-borne burned area products. *Scientific Data*, *5*, 1–12. https://doi.org/10.1038/sdata.2018.132

Lizundia-Loiola, J., Otón, G., Ramo, R., Chuvieco, E. (2020). A spatio-temporal active-fire clustering approach for global burned area mapping at 250 m from MODIS data. Remote Sensing of Environment, 236, 111493. https://doi.org/10.1016/j.rse.2019.111493

Malamud B.D., Morein G., Turcotte D.L. (1998) Forest fires: an example of self-organized critical behaviour. Science 281 (5384), 1840.

Moreno M. V., Laurent P., Ciais P., Mouillot F. (2020). Assessing satellite-derived fire patches with functional diversity trait methods. Remote Sensing of Environment, 247, p. art. 111897, https://doi.org/10.1016/j.rse.2020.111897

Moreno M. V., Laurent P., Mouillot F. (2021). Global intercomparison of functional pyrodiversity from two satellite sensors. International Journal of Remote Sensing, 42 (24), p. 9523-9541, https://doi.org/10.1080/01431161.2021.1999529

Oom, D., Silva, P. C., Bistinas, I., Pereira, J. M. C. (2016). Highlighting biome-specific sensitivity of fire size distributions to time-gap parameter using a new algorithm for fire event individuation. Remote Sensing, *8*(8), 1–15. https://doi.org/10.3390/rs808066

Pettinari M.L., Roteta E. (2021) ESA CCI ECV Fire Disturbance: D2.4.4. Product User Guide – Small Fire Database, version 2.0. Available at: https://climate.esa.int/en/projects/fire/key-documents/

Turcotte D.L., Malamud B.D., Morein G., Newman W.I. (1999) An inverse-cascade model for self-organized critical behaviour. Physica A: Statistical Mechanics and its Applications 268, 629-643, https://doi.org/10.1016/S0378-4371(99)00092-8

van der Werf, G. R., Randerson, J. T., Giglio, L., van Leeuwen, T. T., Chen, Y., Rogers, B. M., Mu, M., van Marle, M. J. E., Morton, D. C., Collatz, G. J., Yokelson, R. J., Kasibhatla, P. S. (2017) Global fire emissions estimates during 1997–2016, Earth Syst. Sci. Data, 9(2), 697–720, https://doi.org/10.5194/essd-9-697-2017

Zheng B., Ciais P., Chevallier F., Chuvieco E., Chen Y., Yang. H. (2021) Increasing forest fire emissions despite the decline in global burned area. Science Advances 7: eabh2646, https://doi.org/10.1126/sciadv.abh2646.

Annex 1: Acronyms and abbreviations

BA	Burned Area
BD	Burned Date
CCI	Climate Change Initiative
CCI_LC	CCI Land Cover product
FireCCI41	MODIS Fire_cci v4.1
FireCCI51	MODIS Fire_cci v5.1
FireCCISFD20	Sentinel-2 SFD Fire_cci v2.0
FP	Fire Patch
FPFT	Fire Patch Functional Trait
FRP	Fire Radiative Power
FRY	FiRe patch morphologY
FSD	Fire Size Distribution
LC	Land Cover
MCD64A1	MODIS Collection 6 Burned Area Product
MODIS	Moderate Resolution Imaging Spectroradiometer
MWCC	Maximal Weakly Connected Component
NRT	Near Real Time
RoS	Rate of Spread
Rsde	Standard deviation ellipse ratio
S.I.	Shape Index
SDE	Standard Deviation Ellipse
SFD	Small Fire Dataset
SHP	Shapefile
SIFP	Single Ignition Fire Patch
SOC	Self-Organized Critically